Article

A Lizardite–HCN Interaction Leading the Increasing of Molecular Complexity in an Alkaline Hydrothermal Scenario: Implications for Origin of Life Studies

Saúl A. Villafañe-Barajas [1], Marta Ruiz-Bermejo [2,*], Pedro Rayo-Pizarroso [2], Santos Gálvez-Martínez [2], Eva Mateo-Martí [2] and María Colín-García [3]

1   Posgrado en Ciencias de la Tierra, Universidad Nacional Autónoma de México, Ciudad Universitaria, Mexico City 04510, Mexico; aquarium@comunidad.unam.mx
2   Departamento de Evolución Molecular, Centro de Astrobiología (CSIC-INTA), Ctra, Torrejón-Ajalvir, km 4, Torrejón de Ardoz, 28850 Madrid, Spain; prayo@cab.inta-csic.es (P.R.-P.); sgalvez@cab.inta-csic.es (S.G.-M.); mateome@cab.inta-csic.es (E.M.-M.)
3   Instituto de Geología, Universidad Nacional Autónoma de México, Ciudad Universitaria, Mexico City 04510, Mexico; mcolin@geologia.unam.mx
*   Correspondence: ruizbm@cab.inta-csic.es; Tel.: +34-915206458; Fax: +34-915206410

Abstract: Hydrogen cyanide, HCN, is considered a fundamental molecule in chemical evolution. The named HCN polymers have been suggested as precursors of important bioorganics. Some novel researches have focused on the role of mineral surfaces in the hydrolysis and/or polymerization of cyanide species, but until now, their role has been unclear. Understanding the role of minerals in chemical evolution processes is crucial because minerals undoubtedly interacted with the organic molecules formed on the early Earth by different process. Therefore, we simulated the probable interactions between HCN and a serpentinite-hosted alkaline hydrothermal system. We studied the effect of serpentinite during the thermolysis of HCN at basic conditions (i.e., HCN 0.15 M, 50 h, 100 °C, pH > 10). The HCN-derived thermal polymer and supernatant formed after treatment were analyzed by several complementary analytical techniques. The results obtained suggest that: (I) the mineral surfaces can act as mediators in the mechanisms of organic molecule production such as the polymerization of HCN; (II) the thermal and physicochemical properties of the HCN polymer produced are affected by the presence of the mineral surface; and (III) serpentinite seems to inhibit the formation of bioorganic molecules compared with the control (without mineral).
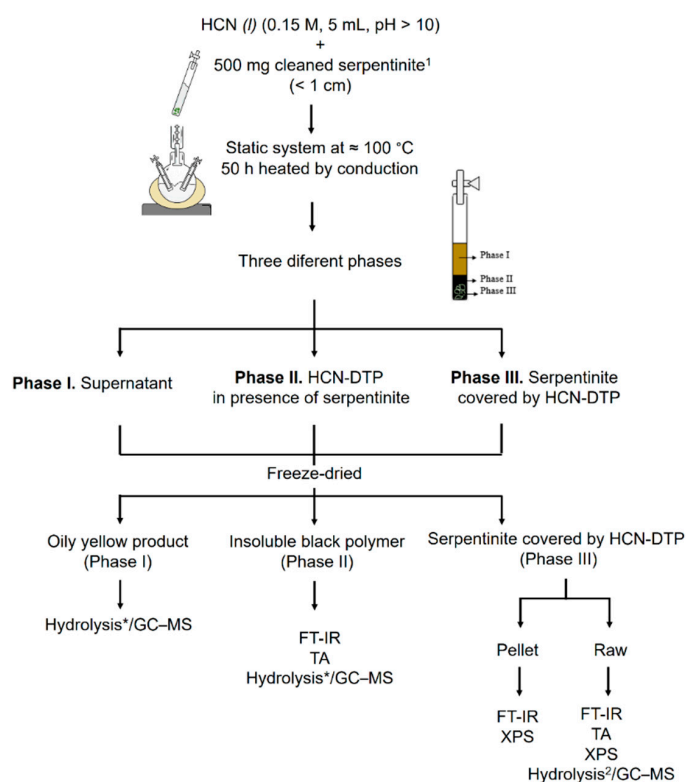
1. Introduction

Currently, it is undoubted that several cyanide species may have had a crucial role in the previous steps for the origin of life [1–3], either as an important source of precursors to building blocks of RNA, proteins, and lipids [4–13] or as important chemical intermediates in phosphorylation reactions [14]. These cyanide species may have been scattered throughout some primitive environments such as the hydrothermal systems, either submarine or subaerial [15–20]. Hydrothermal environments, both subaerial and submarine, are considered ideal systems that allowed chemical evolution on Earth [21–23]. It has been proposed that serpentine-hosted hydrothermal systems may support favorable conditions for prebiotic pathways due to the coexistence of different geochemical variables on them [21,24–26]. Serpentinites are rocks formed mostly of serpentine-group minerals derived from metamorphism of mafic–ultramafic rocks that were abundant during the Hadean–Archean eons [27–30]. In general, these hydrous magnesium silicates are formed after low-temperature (<400 °C) hydration of ferromagnesian or magnesian minerals (e.g., olivine, orthopyroxene) formed in basic and ultrabasic rocks [31].

Because hydrothermal activity and the serpentinization process should have been common and widely distributed in the first 1000 Ma of the Earth's history [24,26,29,32–35], some authors have highlighted the interactions among cyanide species and geochemical variables present in hydrothermal environments and their aftermath in origin of life scenarios [2,36–41].

Recent papers have shown that hydrothermal fluids, during the serpentinization process, can lead to the occurrence of carbonaceous matter on mineral surfaces [42–44]. In addition, it has been shown that alkaline conditions and the dynamic surroundings that are present in hydrothermal systems are crucial for the transformation of cyanide species (e.g., cyanide salts and hydrogen cyanide, HCN) into other organic precursors with interesting roles in pre-RNA world scenarios [11,12,45–48]. Therefore, it seems necessary to study the role of serpentinite during the polymerization of HCN in order to simulate a feasible primitive geochemical scenario such as the surroundings of an alkaline hydrothermal system.

The polymerization of HCN has been widely studied [49–55]; however, few reports have focused on the polymerization of HCN onto mineral surfaces. Ferris et al. [56] found that the presence of montmorillonite inhibits the formation of oligomers because the clay decomposes the tetramer of HCN (i.e., diaminomaleonitrile, DAMN); this effect increases at higher temperatures [47]. However, Boclair and coworkers [57] reported that layered double hydroxides (LDH) can favor the self-addition of cyanide at alkaline pH. On the other hand, the -irradiation of an heterogeneous sample of HCN/Na-montmorillonite inhibited the amount of carboxylic acids formed [58]. In addition, it has been shown that the properties (e.g., structure, kind of deposition, morphology) of aminomalononitrile-based films are modified by the presence of surfaces (e.g., quartz, glass, and silica; [59]). There is no comprehensive information about the role of mineral surfaces during HCN polymerization.

The dynamism of hydrothermal systems offers an interesting place for chemical reactions. For instance, the continuous transport of material along the surroundings of hydrothermal systems (i.e., the vent field that includes all active hydrothermal fluids (both at low (<100 °C) and high temperatures (<400 °C)) may involve the occurrence of thermolysis and polymerization reactions of raw material. Recently, we characterized a polymer formed from the thermolysis of HCN (i.e., HCN-DTP) [46] simulating a simple alkaline hydrothermal system. In this work, using the same synthesis conditions (i.e., $HCN_{(l)}$ 0.15 M, 50 h, 100 °C, pH > 10), we studied the role of serpentinite related to the physicochemical properties of the formed polymer (HCN-DTP/serpentinite) as well as the nature of the supernatant and the mineral coated by an organic layer (Figure 1). Finally, we discuss the implications for chemical evolution studies.

HCN *(l)* (0.15 M, 5 mL, pH > 10)
+
500 mg cleaned serpentinite[1]
(< 1 cm)

Static system at ≈ 100 °C
50 h heated by conduction

Three diferent phases

Phase I
Phase II
Phase III

Phase I. Supernatant

Phase II. HCN-DTP
in presence of serpentinite

Phase III. Serpentinite
covered by HCN-DTP

Freeze-dried

Oily yellow product
(Phase I)

Insoluble black polymer
(Phase II)

Serpentinite covered by HCN-DTP
(Phase III)

Hydrolysis*/GC–MS

FT-IR
TA
Hydrolysis*/GC–MS

Pellet

Raw

FT-IR
XPS

FT-IR
TA
XPS
Hydrolysis[2]/GC–MS

1) Serpentinite was cleaned using KOH 3% v/v; H_2O; HNO_3 3% v/v and characterized using XRD, FT-IR, and TA.

2) The hydrolysis procedure comprised two kinds of hydrolysis: acid (HCl 6N, 100-110 ºC, 16-24 h) and basic (NaOH 0.1N, 100 ºC, 6 h). Both procedures were carried out in each sample.

Figure 1. Processes followed for the synthesis and characterization of the HCN-DTP in presence of serpentinite.

2. Materials and Methods

2.1. Mineral/HCN Samples

Serpentinite was provided by Professor Fernando Ortega-Gutiérrez (Geology Institute, Universidad Nacional Autónoma de México, Ciudad Universitaria, 04510 Cd. Mx, Mexico). The sample was obtained from the Acatlán Complex, SW México [60]. In order to remove all the organic material on the sample, the following procedure was carried out: fragments of mineral (< 1 cm) were washed with a KOH solution (3% *v/v*) for 30 min (1 g mineral/10 mL solution). After that, the mineral was stirred in distilled water (30 min) to remove the KOH excess. Later, the sample was washed with HNO_3 solution (3% *v/v*) (1 g mineral/10 mL solution) for 30 min. Finally, the mineral was cleaned with distilled water to remove the acid excess. Mineral was dried at room temperature. XRD analysis was performed for mineralogical characterization of the serpentinite sample. The lizardite polymorph predominated in the sample. XRD spectra (Figure 2) showed distinctive diffraction peaks corresponding to lizardite (91%), antigorite (5%), and minor traces of magnetite and brucite (≈4%). Lizardite has the structural formula $M_3T_2O_5(OH)_4$, where M is mainly Mg and T is Si, although several common elements can be present in Table 2. Al^{3+}, Ni, Mn^{2+}, or Zn^{2+} [61–63]. In this mineral, 1:1 flat layers of sheets of SiO_4 tetrahedra and sheets of $MgO_2(OH)_4$ octahedra are linked by hydrogen bonds. The most common polytypic is the stacking of three layers without any lateral shift [64].
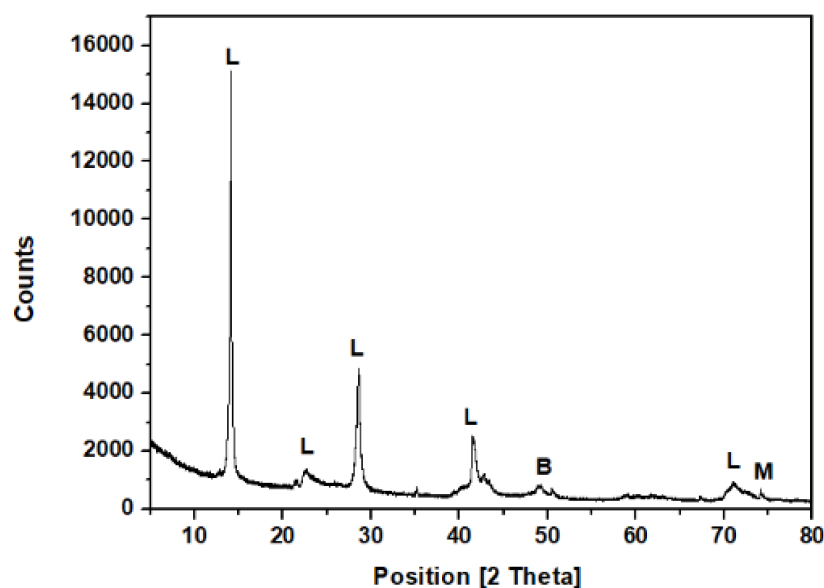
Figure 2. X-ray pattern for the serpentinite rock sample. Diffraction peaks were assigned based on previous works [61,63]. Legend: (L) lizardite $Mg_3Si_2O_5 (OH)_4$, (M) magnetite (Fe_3O_4), and (B) brucite ($Mg(OH)_2$).

To confirm that the mineral sample was not contaminated, a mass spectroscopy thermal analysis was carried out for the cleaned serpentinite sample. Peaks related to OH^- and H_2O (at 619 and 696 °C) were detected; this corroborated that all organic material was removed from the serpentinite (figure not shown).

The HCN-DTP was synthesized in the presence of serpentinite as follows. HCN solution was produced in situ by the reaction between KCN and H_2SO_4 under argon atmosphere (for further details, please see Villafañe-Barajas et al., 2020 [46]). Once the desired concentration was reached (0.15 mol L^{-1}), the pH of the HCN solution was adjusted (pH > 10) with KOH solution (0.1 mol L^{-1}) to favor the availability of ^-CN and the formation of HCN-polymers. Finally, aliquots of HCN solution (0.15 mol L^{-1}, 5 mL) were prepared with 500 mg of the previously cleaned serpentinite in glass tubes and heated in a static system at 100 °C for 50 h. The selected temperature was consistent with the one found in the surroundings of alkaline hydrothermal environments. After treatment, three phases could be distinguished in the sample: I) supernatant (yellow soluble part), II) HCN-DTP (black polymer that was not adhered to mineral surface), and III) mineral + HCN-DTP (serpentinite covered by polymer). The three phases were analyzed by different analytical techniques (for more details, see Figure 1).

2.2. Analysis of Samples

2.2.1. FT-IR Spectroscopy (FT-IR)

The spectra were collected with a FT-IR spectrometer (Nicolet Thermo Fisher ®, model Nexus 67, MA, USA, software OMNIC) using CsI pellets. Using a DRIFT reflectance accessory (Harrik, model Praying Mantis DRP, New York, NY, USA), the spectra of Phases II and III in the 4000–450 cm^{-1} spectral region (spectral resolution of 2 cm^{-1}) were obtained.

2.2.2. Thermal Analysis (TA)

A thermal analysis (thermogravimetry (TG), differential thermal analysis (DTG), and differential scanning calorimetry (DSC)) was performed with a TA instrument® (SDTQ-600/Thermo Star). The method involved operating in isothermal mode (20 min) and a heating ramp of 10 °C min^{-1} until 1000 °C under inert atmosphere (argon, flux 100 mL min^{-1}). The analysis of the main released species along dynamic thermal decomposition from

fragmentation process, were carried out with a coupled TG–MS system using an electron-impact quadrupole mass-selective detector (model Thermostar QMS200 M3).

2.2.3. XPS Spectroscopy Analysis

X-ray photoelectron spectroscopy analysis of Phase III was carried out in an ultrahigh-vacuum chamber equipped with a hemispherical electron analyzer and with the use of an Al Kα X-ray source (1486.6 eV) with an aperture of 7 mm $\times$ 20 mm. The base pressure in the chamber was 3×10^{-8} mbar, and the experiments were performed at room temperature. The sample was analyzed by preparing a pellet containing a sample of approximately 100 mg obtained after grinding and pressing the Phase III (mineral + HCN-DTP). Phase III was also analyzed as raw sample (rock covered by the polymer). The peak analysis in different components was shaped, after background subtraction, as a convolution of Lorenztian and Gaussian curves. Binding energies were calibrated against the binding energy of the C 1s peak at 285.0 eV. Calculation of the atomic relationships between the identified elements was derived from integral peak intensities and sensitivity factors supplied by Handbook of XPS [65].

2.2.4. Hydrolysis and GC–MS Analysis

To conduct a comparative analysis, a basic (NaOH 0.1N, 100 °C, 6 h) and acid (HCl 6N, 110 °C, 24 h) hydrolysis procedure was performed following previous reports [46,66]. After treatment, the samples (Phases I, II, and III) were analyzed by a GC system coupled to a 5975 VL MSD (Agilent®). The detection and characterization of different signals were performed as previously reported [9,46].

3. Results and Discussion

3.1. Fourier Transform Infrared (FT-IR) Spectroscopy

The FT-IR spectra of Phases II and III were registered and compared with their respective control samples. That means that the Phase II was compared to the polymer control HCN-DTP synthesized in the absence of mineral and the Phase III to a control serpentinite sample (Figure 3). This was done as a first step to evaluate the effect of the serpentinite in the cyanide polymerization process.

There were no appreciable differences between the spectra of the mineral alone and the Phase III (Figure 3A). The lack of differences between the naked mineral spectrum and the coated serpentinite is probably because the spectrum of the Phase III was registered using a pellet of the raw sample. As will be discussed below, the organic film represents a very low amount (in % weight) of the raw Phase III. Therefore, in relative proportion, the intensities of the mineral FT-IR features are much higher than those of the organic film; therefore, it was not possible to characterize the polymeric coating by this methodology. The FT-IR spectrum of the serpentinite described here (Figure 3A) is very similar to others spectra previously reported, with characteristic peaks centered at 3682 cm^{-1}, related to MgO-H stretching vibration modes, and at 974 cm^{-1} with a shoulder at 1068 cm^{-1}, corresponding to the Si–O–Si asymmetric stretching mode (for a detailed description of these FT-IR spectra, see, e.g., Rivero Crespo et al., 2019; [67]).
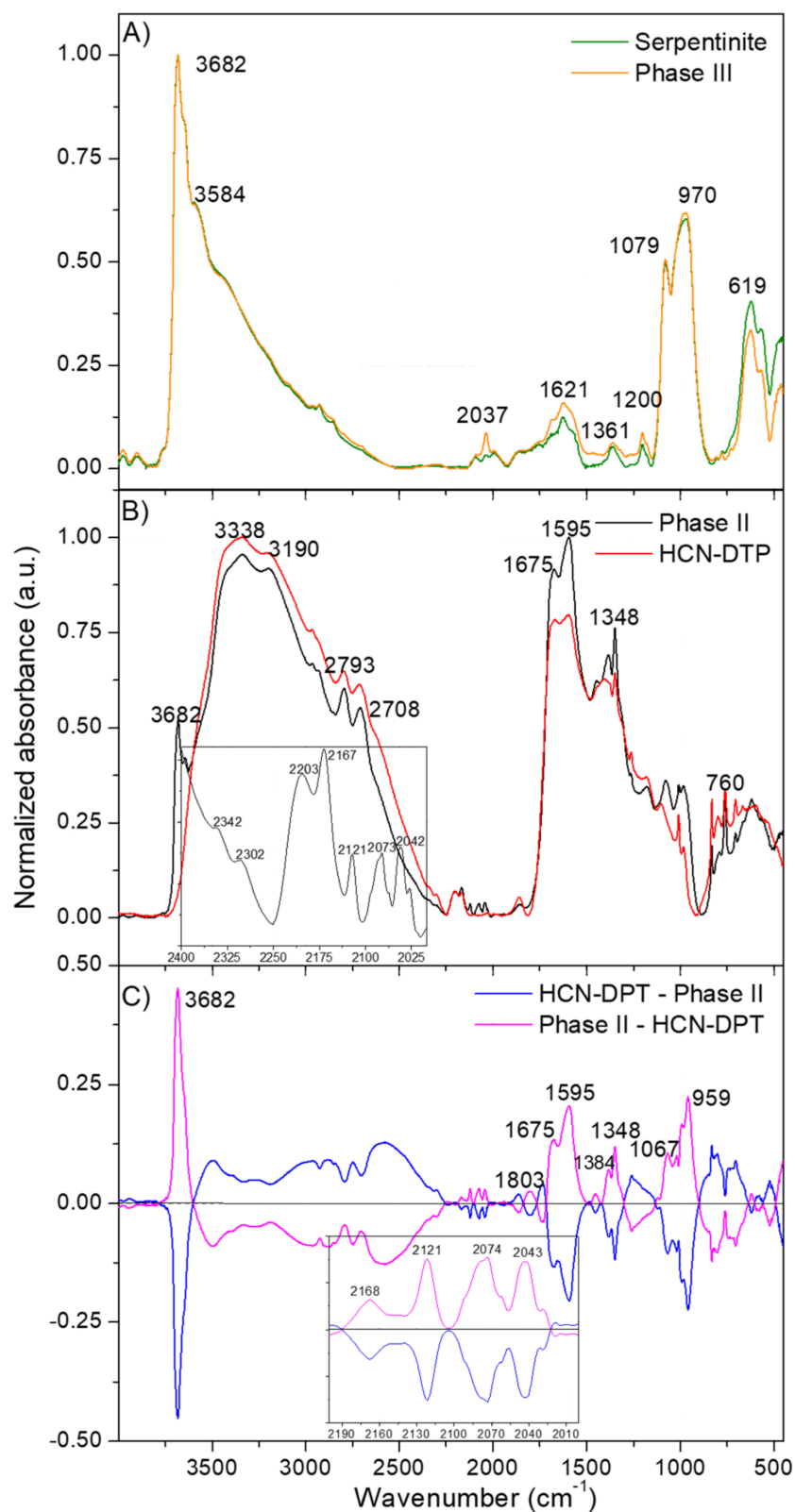
Figure 3. FT-IR spectra of (**A**) net serpentinite (clean control mineral) and serpentinite coated in a HCN-derived polymeric film (Phase III); (**B**) HCN-DTP polymer synthesized in the presence of serpentinite (Phase II) and control HCN-DTP polymer (synthesized in the absence of serpentinite); and (**C**) subtraction of the FT-IR spectra of the Phase II and the control HCN-DTP polymer.

On the other hand, the FT-IR spectra of the Phase II and the polymer control HCN-DTP present the same main features (Figure 3B). Detailed interpretations of these spectra were presented in Villafañe-Barajas et al. [46] indicating the generation of a highly conjugated macrostructure dominated by oxygenated functional groups. However, some slight but significant differences can be observed between the Phase II and the polymer control HCN-DTP (inset plot in Figure 3B and the subtraction of the spectra in Figure 3C). The subtraction of the FT-IR spectra of the Phase II and the polymer control HCN-DTP (pink line in Figure 3C) presents a clear feature at 3682 cm^{-1} and additional features at 959 and 1067 cm^{-1}, which can be related with the presence of residual serpentinite in the Phase II. The bands at 1803, 1675, and 1595 cm^{-1} may indicate a greater oxidation state for the Phase II, since these bands can be assigned to carbonyl compounds such as esters, ketones, amides, and carboxylic acids. Furthermore, the band at 1348 cm^{-1} can be related to -COO^{-} groups in carboxylic acids salts (in this case, the counterions can come from the residual serpentinite). The features centered at 2168, 2121, 2074, and 2043 cm^{-1} identified in the Phase II (inset plot Figure 3C) can be assigned to azide (-N=N=N), carbodiimide (-N=C=N), and isonitrile (N≡C) functional groups. Therefore, it seems that the serpentinite increases the hydrolysis in the HCN polymerization, resulting in highly oxidized products.

3.2. Thermal Analysis

Thermal analysis allowed characterization of the thermal behavior of the samples and finding notable differences between HCN polymers that were not evident using FT-IR spectroscopy. DTG and DSC curves are considered fingerprints to characterize and distinguish among HCN polymers with very similar FT-IR spectra [68,69]. As was done in the previous sections with the FT-IR spectra, the thermal curves of the Phase II were compared with those of the polymer control HCN-DTP and the curves for the Phase III with the control clean serpentinite (Figure 4). In addition, the thermal analysis of the Phase III was carried out under an air atmosphere. In accordance with previous reports, the thermogravimetric behavior of the samples was divided into three stages: I) drying stage (<150 °C), II) pyrolysis stage (150–450 °C), and III) carbonization stage (>450 °C) [46,68–72]. The total weight loss of serpentinite was 12.6%, which agrees with previous reports, together with the DTG doublet in the carbonization stage (Figure 4A,C; Table 1) and with the DTA sharp exothermic peak at 823 °C [73]. The thermal decomposition of this mineral leads to the dehydroxylation of the structure; the bound hydroxyl groups are removed from the serpentinite and liberated as water vapor [74]. The release of these groups reaches its maximum peaks at ~619 and ~696 °C as shown in the DTG curve (Figure 4C; Table 1). Likewise, the DSC and DTA curves (Figures 4E and 5) show a sharp exotherm peak at ~823 °C, which indicates the complete formation of olivine (i.e., forsterite; Mg_2SiO_4) ([74,75].

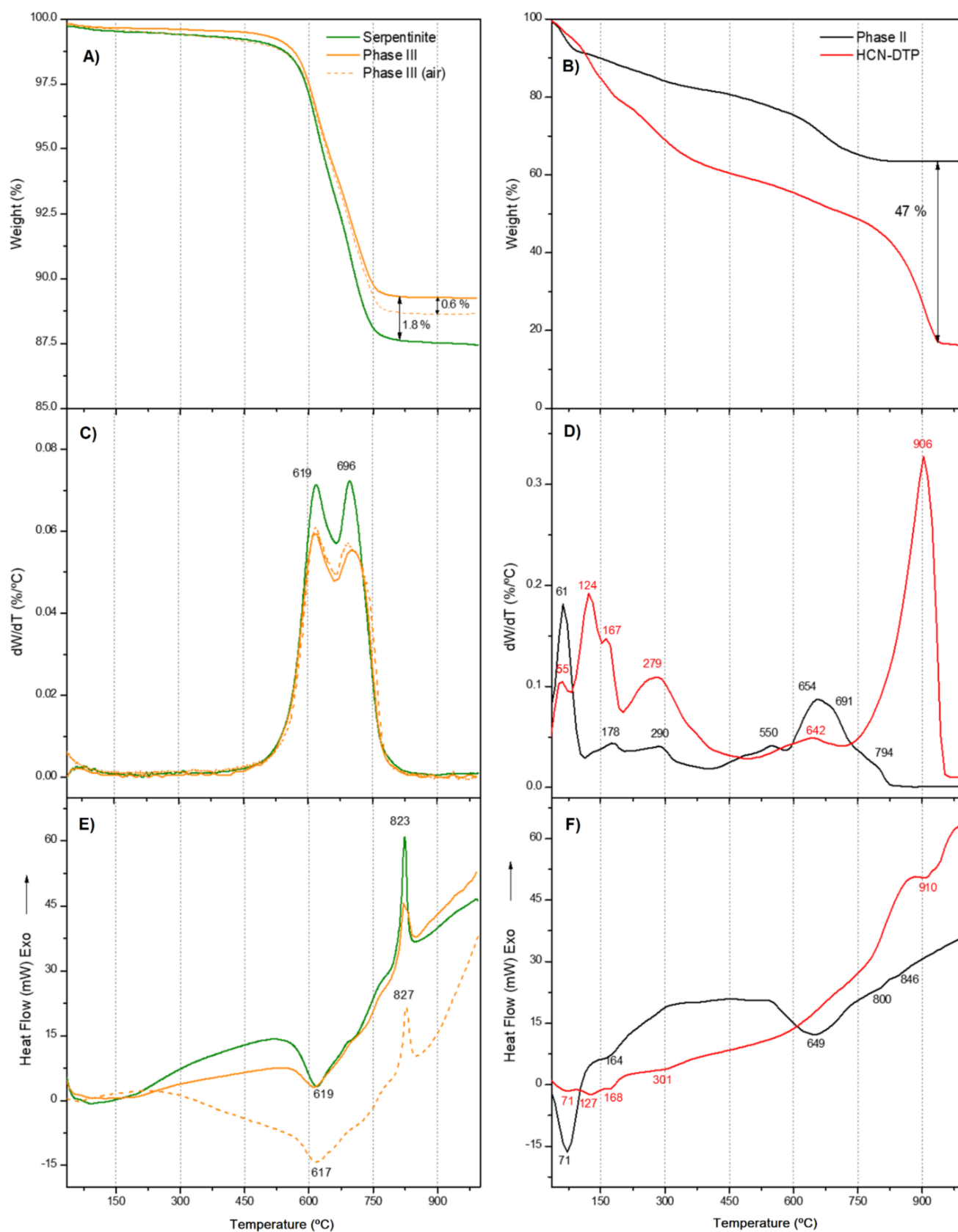**Figure 4.** (**A**) and (**B**) TG curves; (**C**) and (**D**) DTG curves; (**E**) and (**F**) DSC curves. Note that an important amount of residue remained even at high temperatures. The most important decomposition step occurred along the third thermal stage. The identified stages were (I) drying stage (<150 °C), (II) pyrolysis stage (150–450 °C), and (III) carbonization stage (>450 °C).

Table 1. Characteristic temperatures for the thermal decomposition of samples. DTG maxima with the corresponding rates of weight loss, dW/dt, and DSC peaks observed in the samples.

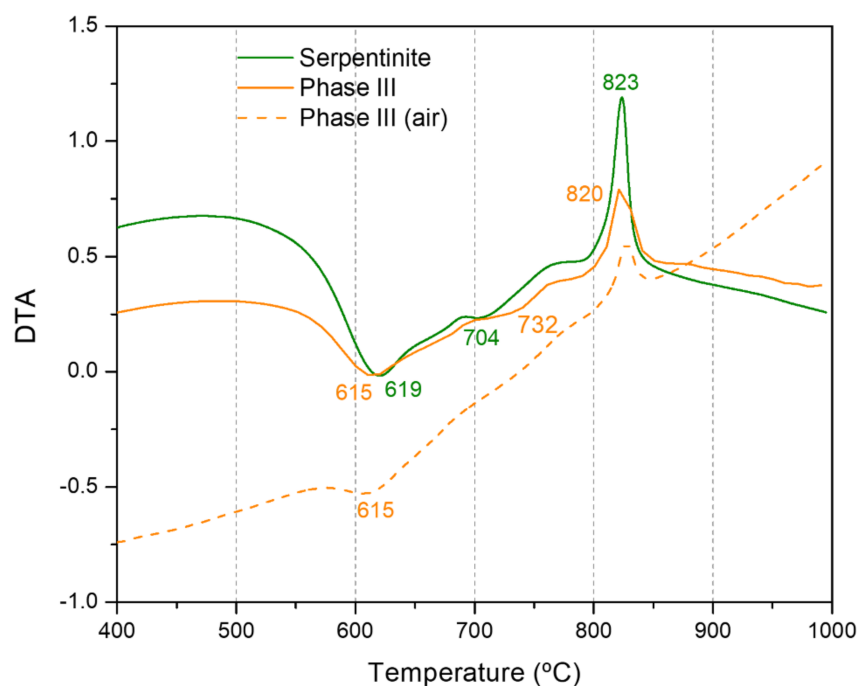| Sample | Stage I (25–150 °C) Evaporation | | | Stage II (150–450 °C) Low Thermal Decomposition | | | Stage III (450–1000 °C) High Thermal Decomposition | | |
| | DTG | | DSC | DTG | | DSC | DTG | | DSC |
	T_{max} (°C)	dW/dt (wt%/°C)	T_{peak} (°C)	T_{max} (°C)	dW/dt (wt%/°C)	T_{peak} (°C)	T_{max} (°C)	dW/dt (wt%/°C)	T_{max} (°C)
Serpentinite							619	0.07	619
							696	0.07	823
Phase II	61	0.18	71	178	0.04	164	550	0.04	649
				290	0.04		654	0.08	
							691	0.07	800
							794	0.03	846
Phase III							619	0.06	619
							696	0.05	823
Phase III (Air)							619	0.06	617
							696	0.05	827
HCN-DTP	55	0.11	71	167	0.15	168	642	0.05	636
	124	0.20	127	279	0.11		906	0.34	910
				288	0.11	301	921	0.27	938

Figure 5. DTA analysis of serpentinite, phase III and phase III (air).

As with the FT-IR analysis, the thermal analysis does not show appreciable differences between the Phase III and serpentinite (Figure 4A,C,E and Figure 5; Table 1). There was a mass loss of only ~2% during the last thermal stage (> 450 °C) (Figure 4A). This suggests that there was not a significant amount of polymer covering the mineral surface, and, in consequence, the thermal profile obtained was dominated by the thermal behavior of serpentinite. However, for the Phase III, the total weight loss was 10.8%, an amount lower than the weight loss for the control sample, the clean serpentinite. Since dehydration is the unique thermal degradation processes for the serpentinite, it seems that the polymeric

coating might partially prevent the release of water. This also would influence the phase change, because a reduction in the exothermicity of the forsterite formation was observed (Figures 4E and 5). In addition, no thermal degradation of the coating was observed in the thermal curves herein considered. The next section discusses that this thermal decomposition seems to be minor. Furthermore, the thermal degradation of the Phase III in the presence of air led to an additional weight loss of 0.6 % compared to the weight loss obtained by heating under Ar atmosphere (Figure 4A). This result can be related to the total degradation of the polymeric coating, indicating a very low organic contribution (relative percentage in weight) from the film covering the mineral.

On the other hand, the presence of air did not affect the thermal behavior of the serpentinite, since there are not great differences between the thermal curves recorded in the presence of air (previously reported) with those recorded using an inert atmosphere of Ar. Nevertheless, the changes observed in the shapes of the DSC and DTA curves of the Phase III registered in the presence of air seem to be due to the polymeric coating, although without highly significant variations with respect to the clean control serpentinite. These results might indicate a physical (physisorption) interaction between the polymeric coating and the mineral surface instead of a strong chemical interaction (chemisorption). This fact is important to elucidate the possible role of the mineral in the full process of the cyanide polymerization and to understand the interaction between the mineral and the organic polymer. To the best our knowledge, this is the first time that the thermal analysis of a covered mineral by a HCN-derived polymer has been described.

In regard to the Phase II, a mass loss of around 10 wt% was observed during the drying stage (<150 °C), which is a consequence of the release of volatile compounds retained in the polymer, predominantly H_2O. This value is consistent with previous reports [46,68,69,72]. In the second stage, the pyrolysis stage (150–450 °C), the mass loss was also 10 wt%. This value is considerably lower than those previously reported (approx. 25 wt%) [46,68,69,72]. This suggests that, as the second thermal stage has been associated with the decomposition of the side groups on the main chain, the polymer has no highly stable side structures. Two clear DTG peaks appear at 174 and 290 °C. Similar peaks also appear in the DTG curve for HCN-DTP (Figure 4B) [46]. In addition, a shoulder around ~135 °C is detected. The third step, the carbonization stage (>450 °C), showed the most significant differences between the Phase II and the HCN-DTP previously synthesized [46]. The sample yield was approximately ~63 wt% of char residues at the end of the ramp temperature. This is unexpectedly high, which is because of the fact that HCN-DTP yields around 15 wt%, while other HCN-derived polymers have 20 wt% [46,68,69,72]. In addition, this value represents almost the double percentage of the original weight reported (i.e., 36.4%) for the black polymer formed by the thermal decomposition of formamide [76]. It seems, as is the case for the coating film (Phase III), that this Phase II is highly thermally stable. Three signals are evident in the DTG curve: first a slight shoulder around 550 °C and then two predominant peaks at 654 and 691 °C. These peaks match with the signals detected in HCN-derived polymers synthesized from NH_4CN and DAMN [72]; however, this does not mean that identical structures are present. For instance, although there is no clear signal after 800 °C, as in other experiments performed at high temperatures (>80 °C) and high concentrations (>0.1 M) [46,72], there is a change in slope that starts at ~800 °C in the sample synthesized in presence of the mineral (Phase II). Finally, the DSC curve of the Phase II shows only three clear endothermic events at 71, 164, and 649 °C (Table 1). These signals correspond to evaporation of the absorbed water and the two main decomposition processes of the polymer [46,72]. Although the FT-IR spectra of the Phase II and the HCN-DTP previously synthesized are essentially alike, the thermal analysis shows important specific thermal fingerprints for each sample. The main difference is shown in the comparison of the DTG curve from Phase II and the HCN-DTP [46], where there is a peak after 900 °C in the control sample. Likewise, the Phase II shows a higher release of volatile species (e.g., H_2O) in the first thermal step (i.e., <70 °C). This considerable difference might be associated with an increment of hydroxyl groups in the polymer as a consequence of interactions with the

serpentinite structure. Also, the high amount of char for the Phase II could be related with a higher degree of oxidation, in agreement with the FT-IR spectra. It has been proposed that an increase in the thermal stability of the HCN-derived polymers is related to a higher content of oxidizing groups in the macrostructures, which eventually leads to an increase in cross-linking [69]. On the other hand, the residual amount of serpentinite in the Phase II may be very small, because its characteristic thermal peaks are not identified in any of the thermal curves (TGA, DTG, or DSC) of the Phase II (Figure 4B,D,F).

3.3. Mass Spectroscopy Thermal Analysis

Serpentinite control, Phase II, and Phase III were analyzed by in situ mass spectrometry (Figure 6) to gain more information about the chemical species released in each thermal step shown in the DTG curves. We considered the same three thermal stages to compare the thermal behavior. The serpentinite control shows only signals associated to OH^- ($m/z = 17$) and H_2O ($m/z = 18$) at 621 and 700 °C, which signals are consistent with the predominant peaks related to the release of hydroxyl groups from serpentinite as is confirmed by the DTG curve (figure not shown) and is in agreement with previous results [73]. Comparatively, the Phase III shows four clear signals. Three of them coincide around ~620 and ~700 °C and could be associated with NH_2 ($m/z = 16$); OH^-, NH_3 ($m/z = 17$); and H_2O, NH_4^+ ($m/z = 18$). In addition, an appreciable signal at 214 °C is related to HCN ($m/z = 27$) (Figure 6A). Since the serpentinite control does not show peaks below 600 °C, the peak at 214 °C can be directly related to the thermal decomposition of the organic coating (Figure 6A). Considering the intensity of these TG–MS data, the amount of coating on the serpentinite is small, though it seems to partially protect the mineral of dehydration. Further works are needed to determine the thickness and the nature of these films synthesized under hydrothermal conditions. Only one previous paper has reported the kinetics of the deposition of AMN-derived polymers, but it did so at room temperature [59] and did not focus on the thermal stability of this new series of coatings.

Table 2. Summary of detected volatile species in Phase II. The MS peaks are associated with each thermal stage. Orange = Stage I. Evaporation (25–150 °C); Blue = Stage II. Low thermal decomposition (150–450 °C); Green = Stage III. High thermal decomposition (450–1000 °C).

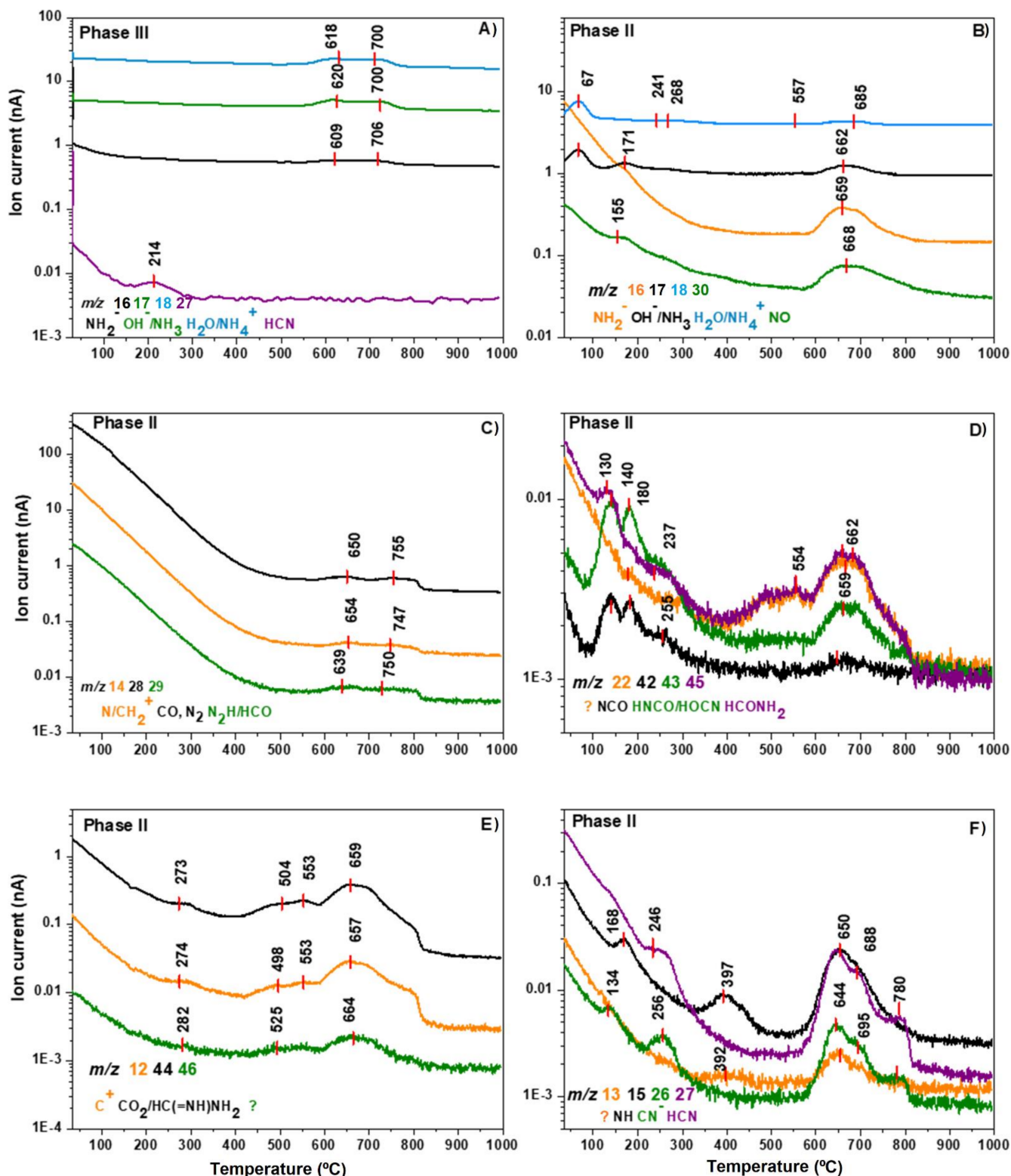| Probable Species	MS Peaks (*m/z*)	TG-MS Peaks for Phase II 62	174	285	550	654
C+	12			Blue	Green	Green
?	13					Green
N,CH$_2$$^+$	14					Green
NH	15		Blue			Green
NH$_2$	16					Green
OH$^-$/NH$_3$	17	Orange	Blue			Green
H$_2$O/NH$_4$+	18	Orange		Blue	Green	Green
?	22				Green	Green
-CN	26		Blue	Blue		Green
HCN	27		Blue	Blue		Green
CO,N$_2$	28					Green
N$_2$H,HCO	29					Green
NO	30		Blue			Green
NCO	42		Blue			Green
HNCO/HOCN	43		Blue	Blue		Green
CO$_2$/ HC(=NH)NH$_2$	44			Blue	Green	Green
HCONH$_2$	45		Blue	Blue		Green
?	46		Blue	Blue		Green
Stage		**I**	**II**		**III**	

Figure 6. Ion intensity curves: (**A**) for Phase III; (**B–F**) for the Phase II. All signals are indicated in Table 2 with their correspondent DTG peaks. The predominant peaks on the third stage are the result of the contribution of several carbon and/or nitrogen species.

Phase II shows several changes related to the signals observed in the HCN-DTP control sample [46]. Figure 6B displays the predominant signals linked to NH_2 ($m/z = 16$; $T = 659\ °C$); OH^-, NH_3 ($m/z = 17$; $T = 67$, 171, and 662 °C); H_2O, NH_4^+ ($m/z = 18$; $T = 67$,

241, 268, 557, and 685 °C); and NO (m/z = 30; T = 155 and 668 °C). Though these species and peaks were also present in the HCN-DTP, the Phase II has new, well-defined signals associated with NH_2, OH^-/NH_3, and NO around ~660 °C. In addition, the m/z = 30 profile does not have the same broad peak around ~160 °C as the control sample (Figure 6B). Two clear peaks are shown for the profiles associated with N/CH_2 (m/z = 14); CO, N_2 (m/z = 28); and N_2H/HCO (m/z = 29) at ~650 and 750 °C (Figure 6C). These signals contribute to the broad peak shown in the DTG curve at the third stage (>450 °C). The thermal profile is totally different, even though these species are released in the HCN-DTP. First, the ion current is considerably higher, and it is thus impossible to identify peaks before 600 °C as is possible in the control sample (e.g., 172 and 283 °C). Moreover, the Phase II does not present peaks after 900 °C as is evident in the HCN-DTP.

In general, the signals in the pyrolysis (150–450 °C) and carbonization stages (>450 °C) are considerably different to the thermal profile of the polymer synthesized in the absence of mineral. The main differences are the predominant peaks around ~660 °C and the absence of peaks after ~900 °C (Figure 6D,E,F). The peaks around ~660 °C are the result of the contribution of several carbon and/or nitrogen species, e.g., C^+ (m/z = 12), NH (m/z = 15), NCO (m/z = 42), HNCO/HOCN (m/z = 43), $CO_2/HC(=NH)NH_2$ (m/z = 44), and $HCONH_2$ (m/z = 45), which suggest the dominance of decarboxylation and/or deamination mechanisms. Other peaks displayed in the same species profiles below 300 °C (e.g., 130, 180, 255, 282) are present in the polymer synthesized without mineral. However, the peaks at 392, 500, and 550 °C are only present for the CH, NH, NCO, $CO_2/HC(=NH)NH_2$, and $HCONH_2$ species in the Phase II (Figure 6E,F). New signals without clear assignments are present in the polymer synthesized in the presence of mineral (e.g., m/z = 13 and m/z =46). Interesting, the profiles associated to cyanide species, CN^- (m/z = 26) and HCN (m/z = 27), are totally different from the control HCN-DTP sample. For instance, the profile of the sample without mineral shows a broad peak that starts at 423 °C and disappears after 900 °C. Instead, in the presence of serpentinite, cyanide species profiles only show three peaks between 640 and 780 °C (Figure 6F). These profiles resemble the general pattern of the DTG curve from the Phase II. Hence, decyanogenation of the polymer takes place mainly at 650 °C. In general, the thermal profile of Phase II shows that decarboxylation, deamination, and/or decyanogenation mechanisms occur mainly around ~660 °C. The absence of this thermal step and the predominant peak after 900 °C in the polymer synthesized without mineral suggest that the presence of serpentinite considerably affects the thermal and structural properties of the HCN-derived thermal polymers. In addition, the possible decyanogenation and degradation process of the Phase III is centered at 214 °C, suggesting a higher thermal lability of the coating than the insoluble black solid, Phase II; this implies that the coating and the insoluble black solid have different structural natures.

Table 2 shows a review of each volatile species contribution related to the thermal stages previously described. In summary, the peak at 124 °C and the two signals after 900 °C do not appear on the DTG curve of the polymer synthesized in the presence of serpentinite. In addition, the serpentinite contributes with an important amount of hydroxyl groups released in the first thermal step (i.e., 62 °C). Finally, the peak around 550 °C is unique in this sample.

3.4. XPS Analysis

The general thermal analysis suggested important physicochemical differences between the HCN-DTP synthesized with and without serpentinite, so X-ray photoelectron spectroscopy analysis was carried out to elucidate the interactions between the organic coating and the mineral surface. Figure 7A shows the photoemission spectra of both the clean serpentinite and the Phase III. The data were registered by using pellets from both samples. The serpentinite control shows clear signals related to its atomic composition (Mg, Si, and O) in strong agreement with previous reports [77]. In this case, the spectra of the clean serpentinite and the Phase III do not show significant chemical changes (Figure 7A). This could be a result of the low amount of organic polymer deposited onto the mineral

surface and diluted in the bulk of the pellet, which may have been insufficient to obtain characteristic or specific signals from the organic film. Some previous studies by our group, where the characterization HCN-derived polymers and *tholins* was performed, reported that ~25% in weight of organic material by total mass of sample (mineral + organic) is necessary [71,78,79] to identify the chemical features of that material without doubt.
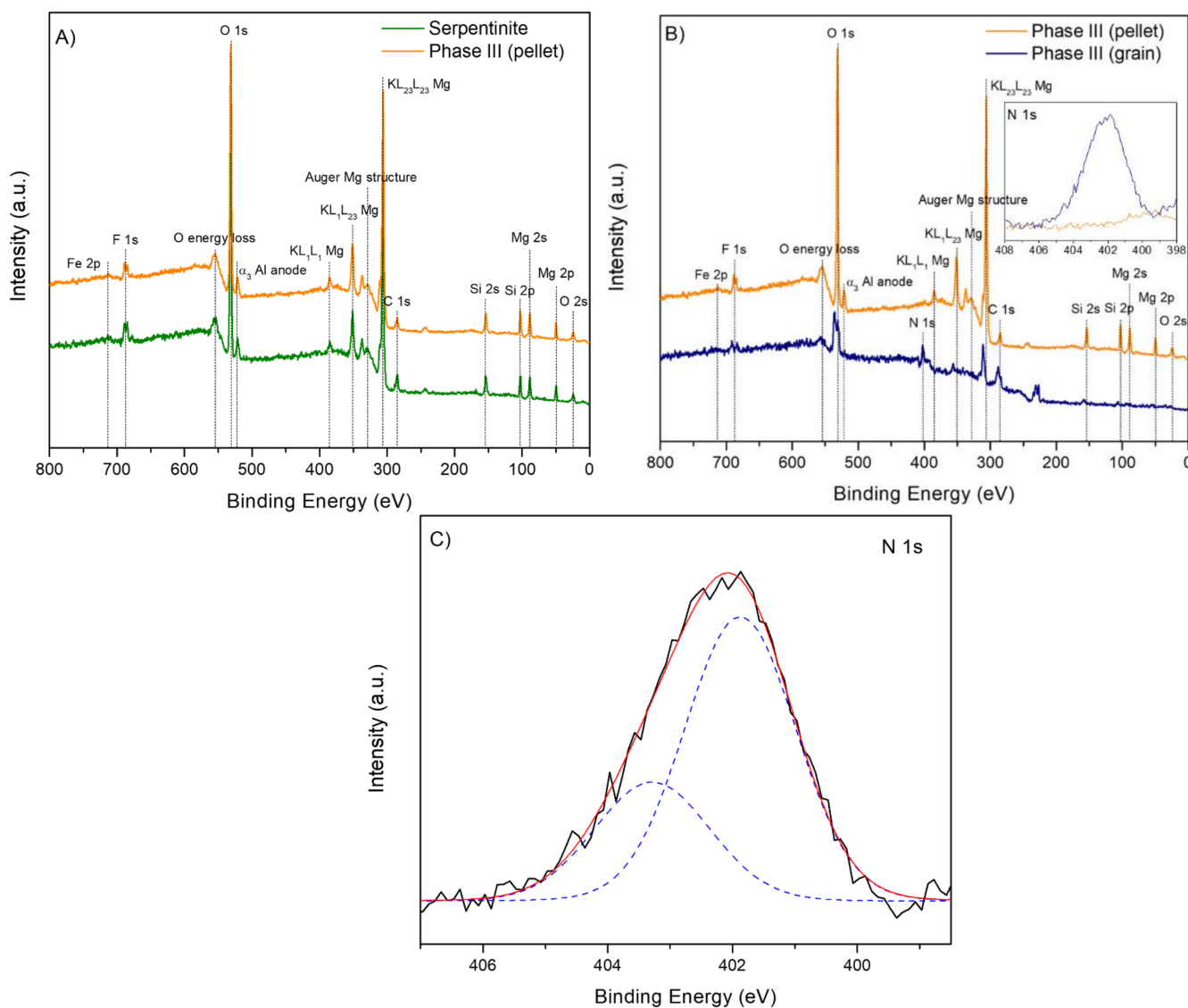

Figure 7. Photoemission spectra of samples. (**A**) XPS overview photoemission spectra of serpentinite control and Phase III (pellet); (**B**) XPS overview photoemission spectra of Phase III (pellet and grain); and (**C**) XPS spectra of N 1s core level peak of Phase III (grain sample), recognized as the fingerprint of the polymeric film.

However, when the XPS spectrum of the Phase III was performed using a coated serpentinite grain, the differences were remarkable (Figure 7B). The main difference among the samples containing an organic coating on the surface is that the mineral signals are attenuated. This can be explained by one main reason: the XPS technique is mainly sensible to the first surface layers of the sample; therefore, once the polymer covers the mineral surface forming a film, the mineral surface stays hidden underneath the organic material. Because of this phenomenon, a signal assigned to N 1s, the fingerprint of the polymeric film, is observed in the Phase III (inset plot in Figure 7B,C). The first component (at 401.8 eV) can be assigned to ammonium cations, and the second one (at 403.3 eV) to azide groups (R-N=N=N-) or nitrites (Figure 7B). The assignation of these components is

different to those of others coatings obtained from AMN at room temperature (although the N 1s signal is significant, Thissen et al. performed deep analysis of C 1s spectra and the binding energies were referenced to aliphatic hydrocarbons peak at 285.0 eV [80] or insoluble cyanide polymers (397.6 eV to imine and/or heterocyclic groups and 398.7 eV to amides [71]. This result is consistent with the fact that the structural nature of the HCN polymers is directly dependent on the experimental synthetic conditions, as well as the chosen monomers used in their syntheses [72]. In the present case, the nature of the mineral substrate could also be considered to explain these differences. Recent works have suggested that the presence of inorganic surfaces (i.e., silica) can affect the properties (e.g., morphology and change of composition film) of AMN-based films [59]. Likewise, Ball [81] reported that AMN-based films deposited on amorphous carbon can affect its electrochemical activity as a consequence of the change in the composition, morphology, and thickness of the film. In addition, he suggested that long deposition times (21 h) produce thicker films. Because our experiments were performing using 50 h of reaction time at a higher temperature, the attenuated XPS signals from the mineral (Figure 7B) may be the consequence of a thick coating that covers the mineral surface. Nevertheless, we cannot discard molecular interactions and/or chemical reactions catalyzed by the mineral between the HCN-DTP and serpentinite once the polymer was formed (e.g., effects of the hydroxyl groups and/or Fe/Mg atoms during polymerization reaction). Additional systematic experiments are needed to understand the real interactions between the HCN polymers and inorganic surfaces. As a result, it seems that there is a physical adsorption of the polymeric coating on the serpentinite mineral, but chemisorption cannot be ruled out. Under the point of view of origin of life studies, these considerations about coating mineral superficies are of interest because they have not been previously taken into account and may increase the chemical space of prebiotic chemistry due to the potential redox properties of these coatings.

3.5. GC–MS Analysis of Hydrolyzed Samples

The dynamism of hydrothermal systems offers important temperature (25–400 °C) and pH gradients (pH = 2–11) along the hydrothermal fields [29,46,82–84]. Hence, the polymers formed in these environments are probably continuously exposed to thermolysis and hydrolysis reactions. Because hydrolysis conditions (i.e., heating time and pH value) are directly related to the amount of organic molecules released [7,66,85], we carried out a hydrolysis procedure (both alkaline and acid hydrolysis at 100–110 °C) for each phase to identify some polar organic compounds associated with each sample. In addition, we compared the detected molecules with those found in the HCN-DTP synthesized in the control experiment (in the absence of serpentine). Figure 8 summarizes all the organic compounds identified in this work.

The predominant species, both in acidic and basic hydrolysis, are glycerol, glycolic acid, succinic acid, orotic acid, stearic acid, and palmitic acid (Figure 9). However, some trends can be distinguished among phases and hydrolysis conditions. For instance, after acidic hydrolysis, carboxylic acids predominated, such as lactic, glycolic, and succinic acid (Figure 9A,C) and only after acid hydrolysis was 2, 5-dihydroxy pyrazine was present. Interestingly, some fatty acids were detected after the basic hydrolysis of the Phase I and II (Figure 9B,D). Related to this, Takahashi and coworkers [86] described the synthesis of fatty acids from HCN using organic solvents and high temperatures (>100 °C). Likewise, Eschenmoser [87] proposed a hypothetical pathway based on the hydrolysis of diamino-maleonitrile (DAMN) and other intermediates previously detected [46] to explain the formation of fatty acids.
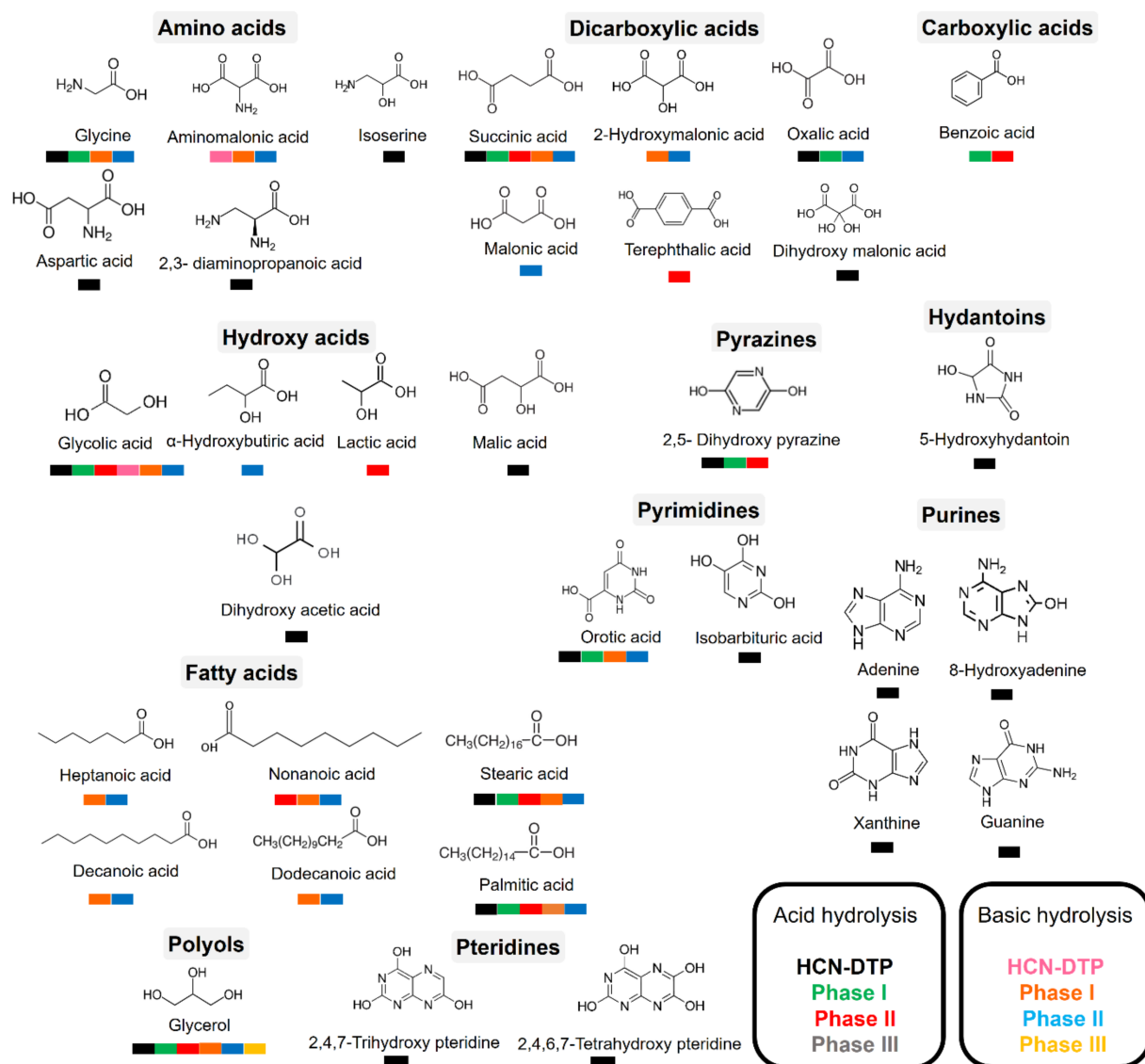
Figure 8. Organic compounds identified in samples after hydrolysis treatments. The colors indicate the sample from which the organic compounds were released.

In basic hydrolysis there was a broader spectrum of hydroxylated species in addition to the species detected by the acid hydrolysis, such as α-hydroxybutiric acid, oxalic acid, malonic acid, hydroxymalonic acid, aminomalonic acid, and other fatty acids (heptanoic acid, decanoic acid, and dodecanoic acid). Carbamate, glycine, orotic acid, and urea were also detected. Notably, in all cases, glycerol was present.

Regarding the Phase III, even using a higher amount of sample (50 mg), there were no clear signals associated with important organic compounds. As mentioned before, this could be a result of the low amount of polymer deposited onto mineral. Only carbamate and glycerol were identified after basic hydrolysis. Thissen et al. [88], in analogous deposition experiments performed on gold substrates, proposed that hydrolysis of imine groups promotes the formation of carbonyl compounds. In our case, the hydrolysis reactions could also lead to the formation of these compounds. Some uncertain signals, probably attributed to alkanes, could be distinguished after acid hydrolysis.
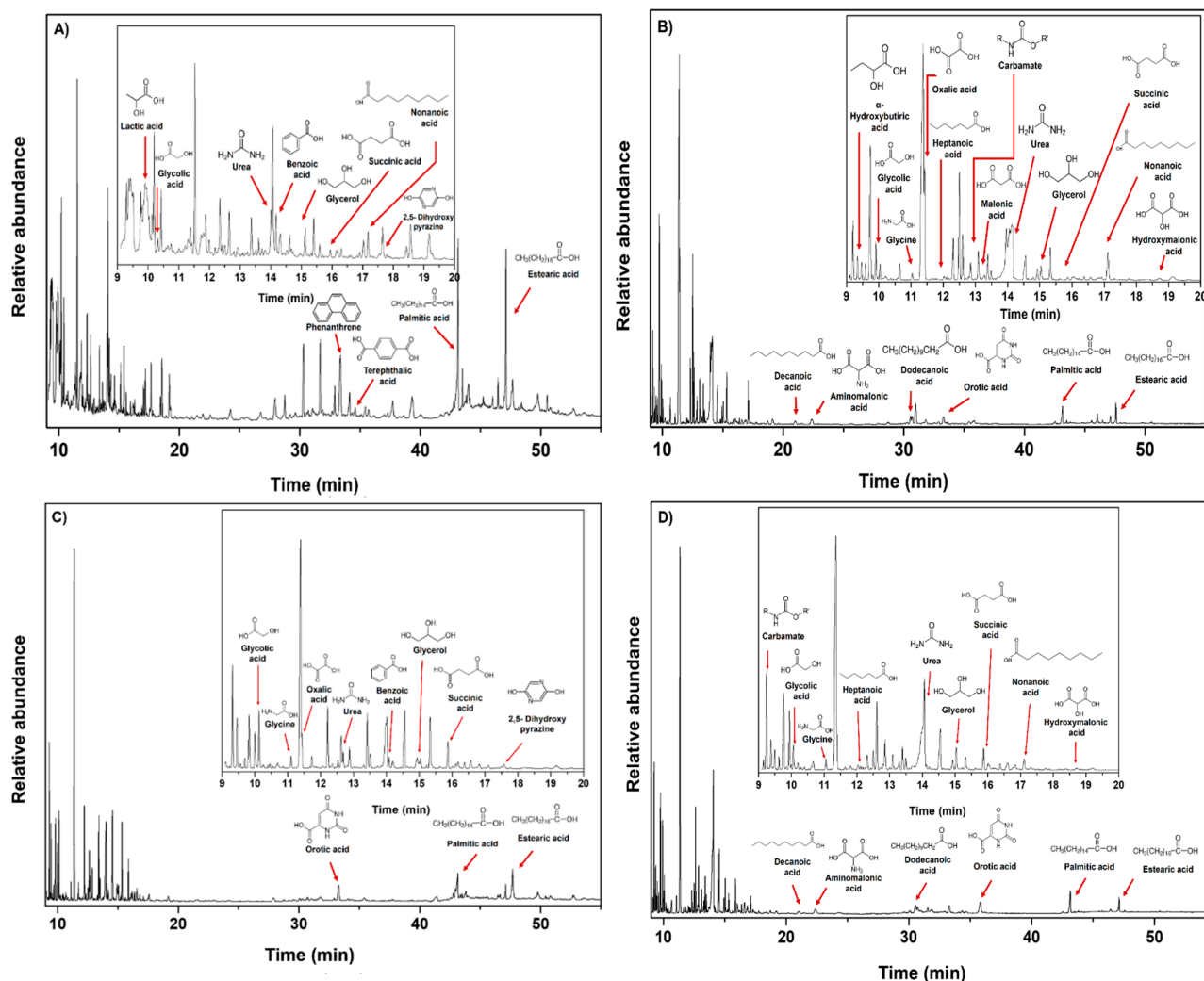
Figure 9. Organic compounds identified in samples after hydrolysis treatments: (**A**) acid hydrolysis for Phase II; (**B**) basic hydrolysis for Phase II; (**C**) acid hydrolysis for Phase I; and (**D**) basic hydrolysis for Phase I. The predominant species, both for acidic and basic hydrolysis, were glycerol, glycolic acid, succinic acid, orotic acid, stearic acid, and palmitic acid.

Minerals could affect the nature of the formed product, even if the exact mechanisms for this are not fully understood. For example, González-López and coworkers [89] found that olivine biases the products formed by thermolysis of acetic acid and formic acid. In our experiments, the presence of serpentinite had interesting repercussions in the diversity of organic molecules detected after hydrolysis treatment (Figures 8 and 9). On the one hand, after acid hydrolysis in presence of mineral, some carboxylic acids, fatty acids, and pyrazine in the Phase I and Phase II were identified. The presence of mineral seems to inhibit the formation of N-heterocyclic compounds, as is evident in the control experiment (HCN-DTP). On the other hand, after basic hydrolysis of samples synthesized in the presence of inorganic surfaces, some amino acids and predominantly fatty acids were released from Phase I and II. Orotic acid was the only cyclic compound detected after both hydrolysis treatments for the samples synthesized in the presence of mineral.

4. Outlook on Studies about Prebiotic Molecular Complexity

The current knowledge about the formation of HCN-derived polymers shows that their features depend on synthesis conditions, including concentration, temperature, presence of oxygen, time of reaction, and raw material [11,46,48,53–55,69,72]. Alkaline hydrothermal systems have been pointed out as very versatile and crucial environments for chemical evolution and, eventually, for origin of life scenarios [38–40,45,90–95]. Con-

sidering the new perspectives of prebiotic chemistry (that suggest to take into account the dynamism of environments, as well as the interactions among their geochemical variables; [29,46,96]), we tested the role of serpentinite during the polymerization of HCN as a first approximation of a simple simulation of an alkaline hydrothermal system. The results suggest that the presence of this mineral affects the thermal properties of HCN-DTP. For instance, the release of volatile species as a function of temperature increment having a maximum peak around ~660 °C is considerably different from the control sample. In addition, some interesting carbon and/or nitrogen volatile species are associated with specific thermal events.

Although the synthesis of organic compounds from serpentinization fluids in ultramafic systems has been reported [97,98], our results suggest that the presence of serpentinite could affect the chemical structure of the formed polymer (in this case HCN-DTP). Hence, it could decrease the diversity of organic molecules released after hydrolysis treatment. Markedly, this inorganic surface inhibited the formation of polar organic compounds and mainly N-heterocyclic compounds, unlike the control experiment (HCN-DTP) [46]. These results raise interesting questions: Is molecular complexity, considering the polymerization of HCN as a prebiotic pathway, reduced in mineral-rich environments? How can the addition of more geochemical variables affect the reactivity of the system? What is the potentiality of these coatings?

Considering the role of minerals in HCN polymerization, previous reports have suggested that montmorillonite inhibits the formation of oligomers [47,56] and reduces the amount of carboxylic acids formed [58]. However, this does not mean that all mineral surfaces may have the same effect. Related to the second question, an interesting study showed that the addition of salts during the HCN polymerization process reduced the diversity of organic molecules, and ammonia had the opposite effect [9]. Compared with similar experiments that simulated alkaline hydrothermal environments using NH_4CN as initial reagent and microwave conditions as energy source, the polar organic compounds identified by the same GC–MS method were considerably lower in our case [48].

On the other hand, the considerable thermal stability of HCN-DTP suggests that its persistence under hydrothermal conditions as well as the presence of coated mineral surfaces could establish new steps in chemical evolution, e.g., acting as semiconductors and catalysts, which are phenomena with important repercussions in the development of new chemical pathways [72] such as photocatalyst reactions [99]. In this way, understanding the properties and roles of these complex materials can shed light about specific catalytic reactions and the formation of some constituents of primitive chemical cycles that were necessary in the first steps of the origin of life [100].

These results indicate that the contribution of different geochemical variables in the same experiment, which tried to simulate the dynamism in these primitive environments, could modify the production of organic compounds. This does not mean a "knock-out" for these systems and their role in chemical evolution. For example, after basic hydrolysis of samples synthesized in presence of serpentinite, the release of some fatty acids is possible. The availability of these molecules and their eventual concentration in microporous matrices of alkaline vents can be enough to precipitate into vesicles [101]. Likewise, depending of pH conditions and salt concentrations, some fatty acid membranes resist extreme environments [102]. On the other hand, even though purines were not synthesized in the presence of mineral, orotic acid was released after hydrolysis treatment (acid and basic). Recently, the importance of orotic acid as a starting point in chemical pathways to RNA has been pointed out [103–105]. Orotic acid can form metal complexes with common ions in hydrothermal conditions (e.g., Cu^{2+}, Mn^{2+}, Zn^{2+}) [106], which complexes could establish new chemical interactions with other organic molecules or surfaces.

5. Conclusions

New perspectives in prebiotic chemistry suggest the necessity of considering the dynamism of primitive environments. Since minerals and organic molecules should have

interacted continuously during early Earth, important phenomena could have developed. Common environments like alkaline hydrothermal systems could have important repercussions in the synthesis and evolution of complex materials such as HCN-DTP and coatings of mineral surfaces. The results suggest that the presence of serpentinite affects the thermal properties of the formed polymer as well the carbon and/or nitrogen volatile species released in specific thermal events. After hydrolysis treatment, several organic molecules with interesting importance in pre-RNA scenarios were identified. Although the effect of mineral surfaces in chemical evolution process has been widely investigated, the focus on coating mineral surfaces is recent. The effect of the presence of mineral surfaces in polymerization reactions and their repercussions in the physicochemical nature of the polymers formed is a new area that introduces a novel vision in prebiotic chemistry.

Author Contributions: Conceptualization, M.R.-B. and M.C.-G.; methodology M.R.-B.; validation, S.A.V.-B., P.R.-P., M.R.-B., and E.M.-M.; formal analysis, S.A.V.-B., P.R.-P., and S.G.-M.; investigation, S.A.V.-B. and S.G.-M.; resources, M.R.-B. and E.M.-M.; writing—original draft preparation, S.A.V.-B., M.R.-B., and M.C.-G; writing—review and editing, M.C.-G.; supervision, M.R.-B. and M.C.-G.; funding acquisition, M.R.-B., M.C.-G., and E.M-.M. All authors have read and agreed to the published version of the manuscript.

Institutional Review Board Statement: No applicable

Informed Consent Statement: Not applicable

Data Availability Statement: Not applicable

Conflicts of Interest: The authors declare no conflict of interest. The funders had no role in the design of the study; in the collection, analyses, or interpretation of data; in the writing of the manuscript, or in the decision to publish the results.

References

1. Ruiz-Bermejo, M.; Zorzano, M.-P.; Osuna-Esteban, S. Simple Organics and Biomonomers Identified in HCN Polymers: An Overview. *Life* **2013**, *3*, 421–448. [CrossRef]
2. Sutherland, J.D. The Origin of Life-Out of the Blue. *Angew. Chem. Int. Ed.* **2016**, *55*, 104–121. [CrossRef]
3. Islam, S.; Powner, M.W. Prebiotic Systems Chemistry: Complexity Overcoming Clutter. *Chem* **2017**, *2*, 470–501. [CrossRef]
4. Powner, M.W.; Gerland, B.; Sutherland, J.D. Synthesis of Activated Pyrimidine Ribonucleotides in Prebiotically Plausible Conditions. *Nature* **2009**, *459*, 239. [CrossRef] [PubMed]
5. Ritson, D.; Sutherland, J.D. Prebiotic Synthesis of Simple Sugars by Photoredox Systems Chemistry. *Nat. Chem.* **2012**, *4*, 895–899. [CrossRef] [PubMed]
6. Ritson, D.J.; Sutherland, J.D. Synthesis of Aldehydic Ribonucleotide and Amino Acid Precursors by Photoredox Chemistry. *Angew. Chem. Int. Ed.* **2013**, *52*, 5845–5847. [CrossRef]
7. Marín-Yaseli, M.R.; Mompeán, C.; Ruiz-Bermejo, M. A Prebiotic Synthesis of Pterins. *Chem. Eur. J.* **2015**, *21*, 13531–13534. [CrossRef] [PubMed]
8. Patel, B.H.; Percivalle, C.; Ritson, D.J.; Duffy, C.D.; Sutherland, J.D. Common Origins of RNA, Protein and Lipid Precursors in a Cyanosulfidic Protometabolism. *Nat. Chem.* **2015**, *7*, 301–307. [CrossRef] [PubMed]
9. Marín-Yaseli, M.R.; González-Toril, E.; Mompeán, C.; Ruiz-Bermejo, M. The Role of Aqueous Aerosols in the "Glyoxylate Scenario": An Experimental Approach. *Chem. Eur. J.* **2016**, *22*, 12785–12799. [CrossRef] [PubMed]

10. Xu, J.; Ritson, D.J.; Ranjan, S.; Todd, Z.R.; Sasselov, D.D.; Sutherland, J.D. Photochemical Reductive Homologation of Hydrogen Cyanide Using Sulfite and Ferrocyanide. *Chem. Commun.* **2018**, *54*, 5566–5569. [CrossRef]

11. Mompeán, C.; Marín-Yaseli, M.R.; Espigares, P.; González-Toril, E.; Zorzano, M.-P.; Ruiz-Bermejo, M. Prebiotic Chemistry in Neutral/Reduced-Alkaline Gas-Liquid Interfaces. *Sci. Rep.* **2019**, *9*, 1–12.

12. Das, T.; Ghule, S.; Vanka, K. Insights into the Origin of Life: Did It Begin from HCN and H_2O? *ACS Cent. Sci.* **2019**, *5*, 1532–1540. [CrossRef]

13. Liu, Z.; Wu, L.-F.; Bond, A.D.; Sutherland, J.D. Photoredox Chemistry in the Synthesis of 2-Aminoazoles Implicated in Prebiotic Nucleic Acid Synthesis. *Chem. Commun.* **2020**, *56*, 13563–13566. [CrossRef] [PubMed]

14. Burcar, B.; Castañeda, A.; Lago, J.; Daniel, M.; Pasek, M.A.; Hud, N.V.; Orlando, T.M.; Menor-Salván, C. A Stark Contrast to Modern Earth: Phosphate Mineral Transformation and Nucleoside Phosphorylation in an Iron- and Cyanide-Rich Early Earth Scenario. *Angew. Chem. Int. Ed.* **2019**, *58*, 16981–16987. [CrossRef] [PubMed]

15. Mukhin, L.E.V. Evolution of Organic Compounds in Volcanic Regions. *Nature* **1974**, *251*, 50–51. [CrossRef]

16. Mukhin, L. Volcanic Processes and Synthesis of Simple Organic Compounds on Primitive Earth. *Orig. Life* **1976**, *7*, 355–368. [CrossRef] [PubMed]

17. Dowler, M.J.; Ingmanson, D.E. Thiocyanate in Red Sea Brine and Its Implications. *Nature* **1979**, *279*, 51–52. [CrossRef]

18. Arrhenius, T.; Arrhenius, G.; Paplawsky, W. Archean Geochemistry of Formaldehyde and Cyanide and the Oligomerization of Cyanohydrin. *Orig. Life Evol. Biosph.* **1994**, *24*, 1–17. [CrossRef]

19. Keefe, A.D.; Miller, S.L. Was Ferrocyanide a Prebiotic Reagent? *Orig. Life Evol. Biosph.* **1996**, *26*, 111–129. [CrossRef]

20. Dzombak, D.A.; Ghosh, R.S.; Wong-Chong, G.M. *Cyanide in Water and Soil: Chemistry, Risk, and Management*; CRC/Taylor & Francis: Boca Raton, FL, USA, 2006.

21. Martin, W.; Baross, J.; Kelley, D.; Russell, M.J. Hydrothermal Vents and the Origin of Life. *Nat. Rev. Microbiol.* **2008**, *11*, 805–814. [CrossRef]

22. Colín-García, M.; Ortega-Gutiérrez, F.; Heredia, A.; Negrón-Mendoza, A.; Ramos-Bernal, S.; Cordero, G.; Camprubí, A.; Beraldi, H. Hydrothermal Vents and Prebiotic Chemistry: A Review. *Boletín Soc. Geológica* **2016**, *68*, 599–620. [CrossRef]

23. Colín-García, M.; Villafañe-Barajas, S.; Camprubí, A.; Ortega-Gutiérrez, F.; Colás, V.; Negrón-Mendoza, A. Prebiotic Chemistry in Hydrothermal Vent Systems. In *Handbook of Astrobiology*, 1st ed.; CRC Press: Boca Raton, FL, USA, 2018; pp. 297–329.

24. Schulte, M.; Blake, D.; Hoehler, T.; McCollom, T. Serpentinization and Its Implications for Life on the Early Earth and Mars. *Astrobiology* **2006**, *6*, 364–376. [CrossRef]

25. Sleep, N.H.; Bird, D.K.; Pope, E.C. Serpentinite and the Dawn of Life. *Philos. Trans. R. Soc. B* **2011**, *366*, 2857–2869. [CrossRef]

26. McCollom, T.M.; Seewald, J.S. Serpentinites, Hydrogen, and Life. *Elements* **2013**, *9*, 129–134. [CrossRef]

27. Müntener, O. Serpentine and Serpentinization: A Link between Planet Formation and Life. *Geology* **2010**, *38*, 959–960. [CrossRef]

28. Arndt, N.T.; Nisbet, E.G. Processes on the Young Earth and the Habitats of Early Life. *Annu. Rev. Earth Planet Sci.* **2012**, *40*, 521–549. [CrossRef]

29. Stüeken, E.E.; Anderson, R.E.; Bowman, J.S.; Brazelton, W.J.; Colangelo-Lillis, J.; Goldman, A.D.; Som, S.M.; Baross, J.A. Did Life Originate from a Global Chemical Reactor? *Geobiology* **2013**, *11*, 101–126. [CrossRef] [PubMed]

30. Schrenk, M.O.; Brazelton, W.J.; Lang, S.Q. Serpentinization, Carbon, and Deep Life. *Rev. Miner. Geochem.* **2013**, *75*, 575–606. [CrossRef]

31. Evans, B.W.; Hattori, K.; Baronnet, A. Serpentinite: What, Why, Where? *Elements* **2013**, *9*, 99–106. [CrossRef]

32. Kelley, D.S. A Serpentinite-Hosted Ecosystem: The Lost City Hydrothermal Field. *Science* **2005**, *307*, 1428–1434. [CrossRef]

33. Shibuya, T.; Komiya, T.; Nakamura, K.; Takai, K.; Maruyama, S. Highly Alkaline, High-Temperature Hydrothermal Fluids in the Early Archean Ocean. *Precambrian Res.* **2010**, *182*, 230–238. [CrossRef]

34. Golding, S.D.; Duck, L.J.; Young, E.; Baublys, K.A.; Glikson, M.; Kamber, B.S. Earliest Seafloor Hydrothermal Systems on Earth: Comparison with Modern Analogues. In *Earliest Life on Earth: Habitats, Environments and Methods of Detection*; Golding, S.D., Glikson, M., Eds.; Springer Netherlands: Dordrecht, The Netherlands, 2011; pp. 15–49.

35. Shibuya, T.; Yoshizaki, M.; Sato, M.; Shimizu, K.; Nakamura, K.; Omori, S.; Suzuki, K.; Takai, K.; Tsunakawa, H.; Maruyama, S. Hydrogen-Rich Hydrothermal Environments in the Hadean Ocean Inferred from Serpentinization of Komatiites at 300 ℃ and 500 Bar. *Prog. Earth Planet. Sci.* **2015**, *2*, 46. [CrossRef]

36. Corliss, J.B.; Baross, J.A.; Hoffman, S.E. An Hypothesis Concerning the Relationships between Submarine Hot Springs and the Origin of Life on Earth. *Oceanol. Acta Spec. Issue* **1981**.

37. Baross, J.A.; Hoffman, S.E. Submarine Hydrothermal Vents and Associated Gradient Environments as Sites for the Origin and Evolution of Life. *Orig. Life Evol. Biosph.* **1985**, *15*, 327–345. [CrossRef]

38. Holm, N.G.; Dumont, M.; Ivarsson, M.; Konn, C. Alkaline Fluid Circulation in Ultramafic Rocks and Formation of Nucleotide Constituents: A Hypothesis. *Geochem. Trans.* **2006**, *7*, 1–7. [CrossRef]

39. Holm, N.G.; Neubeck, A. Reduction of Nitrogen Compounds in Oceanic Basement and Its Implications for HCN Formation and Abiotic Organic Synthesis. *Geochem. Trans.* **2009**, *10*, 1–11. [CrossRef] [PubMed]

40. Rimmer, P.B.; Shorttle, O. Origin of Life's Building Blocks in Carbon-and Nitrogen-Rich Surface Hydrothermal Vents. *Life* **2019**, *9*, 12. [CrossRef]

41. Toner, J.D.; Catling, D.C. Alkaline Lake Settings for Concentrated Prebiotic Cyanide and the Origin of Life. *Geochim. Cosmochim. Acta* **2019**, *260*, 124–132. [CrossRef]

42. Milesi, V.; McCollom, T.M.; Guyot, F. Thermodynamic Constraints on the Formation of Condensed Carbon from Serpentinization Fluids. *Geochim. Cosmochim. Acta* **2016**, *189*, 391–403. [CrossRef]

43. Milesi, V.; Guyot, F.; Brunet, F.; Richard, L.; Recham, N.; Benedetti, M.; Dairou, J.; Prinzhofer, A. Formation of CO2, H2 and Condensed Carbon from Siderite Dissolution in the 200–300°C Range and at 50MPa. *Geochim. Cosmochim. Acta* **2015**, *154*, 201–211. [CrossRef]

44. Sforna, M.C.; Brunelli, D.; Pisapia, C.; Pasini, V.; Malferrari, D.; Ménez, B. Abiotic Formation of Condensed Carbonaceous Matter in the Hydrating Oceanic Crust. *Nat. Commun.* **2018**, *9*, 1–8. [CrossRef]

45. Burcar, B.T.; Barge, L.M.; Trail, D.; Watson, E.B.; Russell, M.J.; McGown, L.B. RNA Oligomerization in Laboratory Analogues of Alkaline Hydrothermal Vent Systems. *Astrobiology* **2015**, *15*, 509–522. [CrossRef]

46. Villafañe-Barajas, S.A.; Ruiz-Bermejo, M.; Rayo-Pizarroso, P.; Colín-García, M. Characterization of HCN-Derived Thermal Polymer: Implications for Chemical Evolution. *Processes* **2020**, *8*, 968. [CrossRef]

47. Villafañe-Barajas, S.A.; Colín-García, M.; Negrón-Mendoza, A.; Ruiz-Bermejo, M. An Experimental Study of the Thermolysis of Hydrogen Cyanide: The Role of Hydrothermal Systems in Chemical Evolution. *Int. J. Astrobiol.* **2020**, 1–10. [CrossRef]

48. Hortal, L.; Pérez-Fernández, C.; de la Fuente, J.L.; Valles, P.; Mateo-Martí, E.; Ruiz-Bermejo, M. A Dual Perspective on the Microwave-Assisted Synthesis of HCN Polymers towards the Chemical Evolution and Design of Functional Materials. *Sci. Rep.* **2020**, *10*, 1–14. [CrossRef]

49. Sanchez, R.A.; Ferris, J.P.; Orgel, L.E. Studies in Prebiotic Synthesis. II. Synthesis of Purine Precursors and Amino Acids from Aqueous Hydrogen Cyanide. *J. Mol. Biol.* **1967**, *30*, 223–253. [PubMed]

50. Ferris, J.P.; Donner, D.B.; Lotz, W. Chemical Evolution. IX. Mechanism of the Oligomerization of Hydrogen Cyanide and Its Possible Role in the Origins of Life. *J. Am. Chem. Soc.* **1972**, *94*, 6968–6974. [CrossRef] [PubMed]

51. Ferris, J.P.; Edelson, E.H. Chemical Evolution. 31. Mechanism of the Condensation of Cyanide to Hydrogen Cyanide Oligomers. *J. Org. Chem.* **1978**, *43*, 3989–3995. [CrossRef]

52. Miyakawa, S.; Cleaves, H.J.; Miller, S.L. The Cold Origin of Life: A. Implications Based on the Hydrolytic Stabilities of Hydrogen Cyanide and Formamide. *Orig. Life Evol. Biosph.* **2002**, *32*, 195–208. [CrossRef]

53. Marín-Yaseli, M.R.; Moreno, M.; de la Fuente, J.L.; Briones, C.; Ruiz-Bermejo, M. Experimental Conditions Affecting the Kinetics of Aqueous HCN Polymerization as Revealed by UV–Vis Spectroscopy. *Spectrochim. Acta A* **2018**, *191*, 389–397. [CrossRef] [PubMed]

54. Fernández, A.; Ruiz-Bermejo, M.; José, L. Modelling the Kinetics and Structural Property Evolution of a Versatile Reaction: Aqueous HCN Polymerization. *Phys. Chem. Chem. Phys.* **2018**, *20*, 17353–17366. [CrossRef]

55. Mas, I.; de la Fuente, J.L.; Ruiz-Bermejo, M. Temperature Effect on Aqueous NH4CN Polymerization: Relationship between Kinetic Behaviour and Structural Properties. *Eur. Polym. J.* **2020**, *132*, 109719. [CrossRef]

56. Ferris, J.P.; Edelson, E.H.; Mount, N.M.; Sullivan, A.E. The Effect of Clays on the Oligomerization of HCN. *J. Mol. Biol.* **1979**, *13*, 317–330. [CrossRef] [PubMed]

57. Boclair, J.W.; Braterman, P.S.; Brister, B.D.; Jiang, J.; Lou, S.; Wang, Z.; Yarberry, F. Cyanide self-addition, controlled adsorption, and other processes at layered double hydroxides. *Orig. Life Evol. Biosph.* **2001**, *31*, 53–69. [CrossRef] [PubMed]

58. Negrón-Mendoza, A.; Ramos-Bernal, S.; Cruz, E.; Juárez, J.M. Radiolysis of HCN in Heterogeneous Phase. *Radiat. Phys. Chem.* **2001**, *61*, 771–772. [CrossRef]

59. Toh, R.J.; Evans, R.; Thissen, H.; Voelcker, N.H.; d'Ischia, M.; Ball, V. Deposition of Aminomalononitrile-Based Films: Kinetics, Chemistry, and Morphology. *Langmuir* **2019**, *35*, 9896–9903. [CrossRef] [PubMed]

60. González-Mancera, G.; Ortega-Gutiérrez, F.; Proenza, J.A.; Atudorei, V. Petrology and Geochemistry of Tehuitzingo Serpentinites (Acatlán Complex, SW Mexico). *Bol. Soc. Geol. Mex.* **2009**, *61*, 419–435. [CrossRef]

61. Rucklidge, J.C.; Zussman, J. The Crystal Structure of the Serpentine Mineral, Lizardite Mg3Si2O5(OH)4. *Acta Cryst.* **1965**, *19*, 381–389. [CrossRef]

62. Mellini, M. Crystal Structure of Lizardite 1T. *Acta Cryst. Sect. A Found. Crystallogr.* **1981**, *37*, C189. [CrossRef]

63. Zheng, S.M.; Wang, K.M. Preparation and Characterization of Lizardite. *AMM* **2014**, *556–562*, 109–112. [CrossRef]

64. Carmignano, O.R.D.; Vieira, S.S.; Brandão, P.R.G.; Bertoli, A.C.; Lago, R.M. Serpentinites: Mineral Structure, Properties and Technological Applications. *J. Braz. Chem. Soc.* **2020**, *31*, 2–14. [CrossRef]

65. Chastain, J.; King, R.C., Jr. Handbook of X-Ray Photoelectron Spectroscopy. *Perkin-Elmer Corp.* **1992**, *40*, 221.

66. Ferris, J.P.; Wos, J.D.; Nooner, D.W.; Oró, J. Chemical Evolution: XXI. The Amino Acids Released on Hydrolysis of HCN Oligomers. *J. Mol. Evol.* **1974**, *3*, 225–231. [CrossRef]

67. Rivero Crespo, M.A.; Pereira Gómez, D.; Villa García, M.V.; Gallardo Amores, J.M.; Sánchez Escribano, V. Characterization of Serpentines from Different Regions by Transmission Electron Microscopy, X-ray Diffraction, BET Specific Surface Area and Vibrational and Electronic Spectroscopy. *Fibers* **2019**, *7*, 47. [CrossRef]

68. de la Fuente, J.L.; Ruiz-Bermejo, M.; Nna-Mvondo, D.; Minard, R.D. Further Progress into the Thermal Characterization of HCN Polymers. *Polym. Degrad. Stab.* **2014**, *110*, 241–251. [CrossRef]

69. Ruiz-Bermejo, M.; José, L.; Marín-Yaseli, M.R. The Influence of Reaction Conditions in Aqueous HCN Polymerization on the Polymer Thermal Degradation Properties. *J. Anal. Appl. Pyrolysis.* **2017**, *124*, 103–112. [CrossRef]

70. de la Fuente, J.L.; Ruiz-Bermejo, M.; Menor-Salván, C.; Osuna-Esteban, S. Thermal Characterization of HCN Polymers by TG–MS, TG, DTA and DSC Methods. *Polym. Degrad. Stabil.* **2011**, *96*, 943–948. [CrossRef]

71. Ruiz-Bermejo, M.; de la Fuente, J.L.; Rogero, C.; Menor-Salván, C.; Osuna-Esteban, S.; Martín-Gago, J.A. New Insights into the Characterization of 'Insoluble Black HCN Polymers. *Chem. Biodivers.* **2012**, *9*, 25–40. [CrossRef] [PubMed]
72. Ruiz-Bermejo, M.; José, L.; Carretero-González, J.; García-Fernández, L.; Aguilar, M.R. A Comparative Study on HCN Polymers Synthesized by Polymerization of NH$_4$CN or Diaminomaleonitrile in Aqueous Media: New Perspectives for Prebiotic Chemistry and Materials Science. *Chem. Eur. J.* **2019**, *25*, 11437–11455. [CrossRef]
73. Viti, C. Serpentine Minerals Discrimination by Thermal Analysis. *Am. Min.* **2010**, *95*, 631–638. [CrossRef]
74. Dlugogorski, B.Z.; Balucan, R.D. Dehydroxylation of Serpentine Minerals: Implications for Mineral Carbonation. *Renew. Sustain. Energy Rev.* **2014**, *31*, 353–367. [CrossRef]
75. Hršak, D.; Sučik, G.; Lazić, L. The Thermophysical Properties of Serpentinite. *Metalurgija* **2008**, *47*, 29–31.
76. Cataldo, F.; Lilla, E.; Ursini, O.; Angelini, G. TGA–FT-IR Study of Pyrolysis of Poly (Hydrogen Cyanide) Synthesized from Thermal Decomposition of Formamide. Implications in Cometary Emissions. *J. Anal. Appl. Pyrol.* **2010**, *87*, 34–44. [CrossRef]
77. Schulze, R.K.; Hill, M.A.; Field, R.D.; Papin, P.A.; Hanrahan, R.J.; Byler, D.D. Characterization of Carbonated Serpentine Using XPS and TEM. *Energ. Convers. Manag.* **2004**, *45*, 3169–3179. [CrossRef]
78. Ruiz-Bermejo, M.; Menor-Salván, C.; Mateo-Martí, E.; Osuna-Esteban, S.; Martín-Gago, J.Á.; Veintemillas-Verdaguer, S. CH$_4$/N$_2$/H$_2$ Spark Hydrophilic Tholins: A Systematic Approach to the Characterization of Tholins. *Icarus* **2008**, *198*, 232–241. [CrossRef]
79. Ruiz-Bermejo, M.; Menor-Salván, C.; de la Fuente, J.L.; Mateo-Martí, E.; Osuna-Esteban, S.; Martín-Gago, J.Á.; Veintemillas-Verdaguer, S. CH$_4$/N$_2$/H$_2$-Spark Hydrophobic Tholins: A Systematic Approach to the Characterisation of Tholins. Part II. *Icarus* **2009**, *204*, 672–680. [CrossRef]
80. Thissen, H.; Koegler, A.; Salwiczek, M.; Easton, C.D.; Qu, Y.; Lithgow, T.; Evans, R.A. Prebiotic-Chemistry Inspired Polymer Coatings for Biomedical and Material Science Applications. *NPG Asia Mater.* **2015**, *7*, e225. [CrossRef]
81. Ball, V. Antioxidant Activity of Films Inspired by Prebiotic Chemistry. *Mater. Lett.* **2021**, *285*, 129050. [CrossRef]
82. Little, S.A.; Stolzenbach, K.D.; Von Herzen, R.P. Measurements of Plume Flow from a Hydrothermal Vent Field. *J. Geophys. Res.* **1987**, *92*, 2587–2596. [CrossRef]
83. Holm, N.G.; Hennet, R.J.-C. Hydrothermal systems: their varieties, dynamics, and suitability for prebiotic chemistry. In *Marine Hydrothermal Systems and the Origin of Life*; Springer: Berlin, Germania, 1992; pp. 15–31.
84. Bemis, K.; Lowell, R.; Farough, A. Diffuse Flow On and Around Hydrothermal Vents at Mid-Ocean Ridges. *Oceanog* **2012**, *25*, 182–191. [CrossRef]
85. Borquez, E.; Cleaves, H.J.; Lazcano, A.; Miller, S.L. An Investigation of Prebiotic Purine Synthesis from the Hydrolysis of HCN Polymers. *Orig. Life Evol. Biosph.* **2005**, *35*, 79–90. [CrossRef]
86. Takahashi, T.; Ido, T.; Hatano, K.; Iwata, R.; Nakanishi, H. Synthesis of 1-11C-Labeled Fatty Acid from [11C]HCN. *Int. J. Rad. Appl. Instr. A* **1990**, *41*, 649–654. [CrossRef]
87. Eschenmoser, A. On a Hypothetical Generational Relationship between HCN and Constituents of the Reductive Citric Acid Cycle. *Chem. Biodivers.* **2007**, *4*, 554–573. [CrossRef]
88. Thissen, H.; Evans, R.A.; Ball, V. Films and Materials Derived from Aminomalononitrile. *Processes* **2021**, *9*, 82. [CrossRef]
89. González-López, L.A.; Colín-García, M.; Meléndez-López, A.; Cruz-Castañeda, J.; Negrón-Mendoza, A. Prebiotic Experi-Ments Simulating Hydrothermal Vents: Influence of Olivine in the Decomposition of Simple Carboxylic Acids. *Bol. Soc. Geológ. Mex* **2021**, in press. [CrossRef]
90. Herschy, B.; Whicher, A.; Camprubi, E.; Watson, C.; Dartnell, L.; Ward, J.; Evans, J.R.G.; Lane, N. An Origin-of-Life Reactor to Simulate Alkaline Hydrothermal Vents. *J. Mol. Evol.* **2014**, *79*, 213–227. [CrossRef]
91. Sojo, V.; Herschy, B.; Whicher, A.; Camprubí, E.; Lane, N. The Origin of Life in Alkaline Hydrothermal Vents. *Astrobiology* **2016**, *16*, 181–197. [CrossRef] [PubMed]
92. Camprubí, E.; de Leeuw, J.W.; House, C.H.; Raulin, F.; Russell, M.J.; Spang, A.; Tirumalai, M.R.; Westall, F. The Emergence of Life. *Space Sci. Rev.* **2019**, *215*, 56. [CrossRef]
93. Damer, B.; Deamer, D. The Hot Spring Hypothesis for an Origin of Life. *Astrobiology* **2020**, *20*, 429–452. [CrossRef]
94. Duval, S.; Branscomb, E.; Trolard, F.; Bourrié, G.; Grauby, O.; Heresanu, V.; Schoepp-Cothenet, B.; Zuchan, K.; Russell, M.J.; Nitschke, W. On the Why's and How's of Clay Minerals' Importance in Life's Emergence. *Appl. Clay Sci.* **2020**, *195*, 105737. [CrossRef]
95. Deamer, D. Where Did Life Begin? Testing Ideas in Prebiotic Analogue Conditions. *Life* **2021**, *11*, 134. [CrossRef]
96. Dass, A.V.; Hickman-Lewis, K.; Brack, A.; Kee, T.P.; Westall, F. Stochastic Prebiotic Chemistry within Realistic Geological Systems. *Chem. Sel.* **2016**, *1*, 4906–4926. [CrossRef]
97. Konn, C.; Charlou, J.L.; Holm, N.G.; Mousis, O. The Production of Methane, Hydrogen, and Organic Compounds in Ultramafic-Hosted Hydrothermal Vents of the Mid-Atlantic Ridge. *Astrobiology* **2015**, *15*, 381–399. [CrossRef]
98. McDermott, J.M.; Seewald, J.S.; German, C.R.; Sylva, S.P. Pathways for Abiotic Organic Synthesis at Submarine Hydrothermal Fields. *Proc. Natl. Acad. Sci. USA* **2015**, *112*, 7668–7672. [CrossRef] [PubMed]
99. Yang, Q.; Peng, P.; Xiang, Z. Covalent Organic Polymer Modified TiO 2 Nanosheets as Highly Efficient Photocatalysts for Hydrogen Generation. *Chem. Eng. Sci.* **2017**, *162*, 33–40. [CrossRef]
100. Eschenmoser, A. The Search for the Chemistry of Life's Origin. *Tetrahedron* **2007**, *63*, 12821–12844. [CrossRef]

101. Budin, I.; Bruckner, R.J.; Szostak, J.W. Formation of Protocell-like Vesicles in a Thermal Diffusion Column. *J. Am. Chem. Soc.* **2009**, *131*, 9628–9629. [CrossRef]

102. Namani, T.; Deamer, D.W. Stability of Model Membranes in Extreme Environments. *Orig. Life Evol. Biosph.* **2008**, *38*, 329–341. [CrossRef]

103. Kim, E.-K.; Martin, V.; Krishnamurthy, R. Orotidine-Containing RNA: Implications for the Hierarchical Selection (Systems Chemistry Emergence) of RNA. *Chem. Eur. J.* **2017**, *23*, 12668–12675. [CrossRef]

104. Krishnamurthy, R. Life's Biological Chemistry: A Destiny or Destination Starting from Prebiotic Chemistry? *Chem. Eur. J.* **2018**, *24*, 16708–16715. [CrossRef] [PubMed]

105. Yadav, M.; Kumar, R.; Krishnamurthy, R. Chemistry of Abiotic Nucleotide Synthesis. *Chem. Rev.* **2020**, *120*, 4766–4805. [CrossRef] [PubMed]

106. Maistralis, G.; Koutsodimou, A.; Katsaros, N. Transition metal orotic acid complexes. *Transit. Met. Chem.* **2000**, *25*, 166–173. [CrossRef]